JOURNAL OF AIRCRAFT
Vol. 32, No. 6, November–December 1995

Transonic Aeroelastic Models of Highly Swept Hypersonic Lifting Surfaces

Edmund Pendleton* and Greg Moster*
U.S. Air Force Wright Laboratory, Wright–Patterson Air Force Base, Ohio 45433
and
Donald Keller†
NASA Langley Research Center, Hampton, Virginia 23681

Transonic aeroelastic wind-tunnel models simulating geometric and dynamic properties of lightweight, highly swept hypersonic lifting surfaces have been designed, fabricated, and tested. The aeroelastic model designs were consistent with preliminary designs of lifting surfaces for single-stage-to-orbit vehicles. The models were tested in the NASA Langley Research Center's Transonic Dynamics Tunnel. This article summarizes the design and tests conducted for each of the two models. Wind-tunnel test results are presented showing aeroelastic instability boundaries. Aeroelastic analyses, conducted for correlation with wind-tunnel results, are also presented.

Introduction

RECENT efforts in the development of hypersonic vehicles have been directed toward the development of a single-stage-to-orbit vehicle that travels through the atmosphere at subsonic to hypersonic speeds. Analyses and some experimental data[1,2] show that this class of vehicles can experience aeroelastic instabilities, particularly in the transonic region. The models described in this article were developed to provide an understanding of the transonic aeroelastic characteristics of single-stage-to-orbit hypersonic lifting surfaces. The first model described is based upon the preliminary design of a lightweight hypersonic horizontal lifting surface stabilator. The second model described is based upon a lightweight hypersonic vertical lifting surface stabilizer and rudder. Descriptions of the design, fabrication, ground tests, aeroelastic analyses, and wind-tunnel test results are provided for each low AR transonic aeroelastic model.

Horizontal Lifting Surface Model

The transonic horizontal lifting surface model consists of a stabilator lifting surface with scaled mass and stiffness properties, a spindle, a splitter plate, and instrumentation. The stabilator has a 70-deg leading-edge sweep and a 22-deg trailing-edge sweep with a pitch pivot boundary condition at the root. The stabilator airfoil is symmetric with leading and trailing edges modeled as sharp edges that taper to a maximum wing thickness to chord ratio of 4.0%.

The stabilator model is attached at the model root to the spindle. A 0.1-in. air gap exists between the model root and the model's splitter plate. Attachment fittings located at 50 and 65% root chord permit the spindle axis of rotation location at the stabilator root to be adjusted. The stabilator spindle passes through the 65% root chord and the splitter plate and into a housing. The spindle housing, located behind the splitter plate, contains two sets of bearings that restrain the spindle to only the pitch degree of freedom. The model pitch degree of freedom is limited to 15 deg positive to 15 deg negative, or can be locked out.

A variable stiffness spring assembly simulating actuator spring stiffness restrains the inboard end of the spindle. The housing is built to be positioned on the wind-tunnel turntable for model angle-of-attack adjustment. The splitter plate is mounted to the wind-tunnel wall using a series of brackets and has 45-deg swept leading edges to reduce the possibility of choked tunnel flow. The splitter plate was utilized during wind-tunnel tests for both lifting surface models. Figure 1 shows the model and the splitter plate.

Aeroelastic Design

The stabilator geometry, mass, and stiffness were scaled from a full-scale NASA structural analysis (NASTRAN[3]) finite element model representation. The stabilator aeroelastic wind-tunnel model design, shown in Fig. 2, was laid out based upon engineering procedures typical of beam-type aeroelastic models. The model design selected relied on aluminum spars, simulating the wing's elastic stiffness, to support a chordwise aerodynamic sleeve constructed of balsa wood. The balsa formed the wing contour to provide proper aerodynamic forces and, in combination with ballast weights, simulated the scaled inertial characteristics. Model scaling levels were set to achieve an aeroelastic instability within the NASA Langley 16-ft Transonic Dynamics Tunnel (TDT) Freon test envelope.

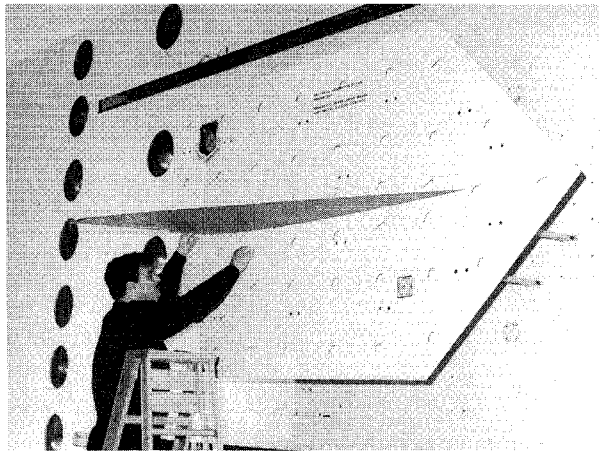

Fig. 1 Horizontal lifting surface model in the wind tunnel.

Received Feb. 28, 1994; presented as Paper 94-1489 at the AIAA 35th Structures, Structural Dynamics, and Materials Conference, Hilton Head, SC, April 18–20, 1994; revision received March 10, 1995; accepted for publication March 16, 1995. This paper is declared a work of the U.S. Government and is not subject to copyright protection in the United States.

*Aerospace Engineer, Flight Dynamics Directorate.
†Aerospace Engineer, Aeroelasticity Configuration Branch.

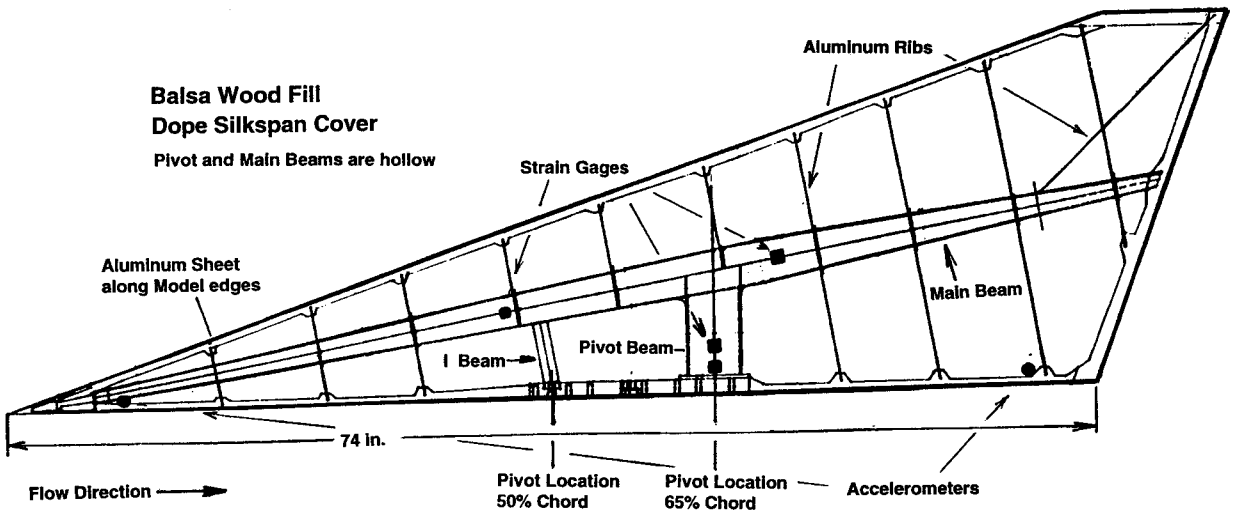

Fig. 2 Stabilator aeroelastic model structural layout.

The stiffnesses of the wind-tunnel model's primary beams were determined from stiffness characteristics present in the full-scale finite element description. Deflections due to unit loads were computed along the wing from the root leading edge to the stabilator aft end. Deflections were also computed from the root at 65% chord outboard to the leading-edge attachment line. The beams' stiffness levels were computed using the beam equations[4] and scaled using the scaling rules.[5,6]

The model's stiffness levels were adjusted through three design iterations. The first design (design I) resulted in a close simulation of the full-scale finite element representation. The second design (design II) contained adjustments to the first design iteration's primary beam's stiffness levels to make beam construction practical. The third design iteration (design III) contained adjustments to the stabilator pivot to make it practical. This final design improved upon the initial design of the wind-tunnel model pivot shaft. The initial design included a very weak flexible spring that reflected the original spindle found in the full-scale finite element model, but was unable to withstand any reasonable airloads in the wind tunnel. Therefore, a pivot spring was designed that could withstand maximum wind-tunnel airloads up to 7-deg angle of attack. The beam stiffness levels were also adjusted in the final design to compensate for the stiffness added by the continuous balsa aerodynamic sleeve. Preliminary stiffness tests conducted on a model specimen revealed the balsa sleeve added approximately 9% to the model's stiffness.

The location of the model's two primary beams is shown in Fig. 2. The beams were designed and constructed with hollow cross sections to achieve the stabilator stiffness and to meet the lightweight stabilator mass properties. Aluminum 6061 was selected as the beam material since it is light, strong, and weldable.

Table 1 gives the required values of area moments of inertia I, and polar moments of inertia J, for the two primary beams. Two sets of required torsional stiffness values are shown for the main beam. The first set depicts stiffness values determined from the first design iteration. The second set reflects practical stiffness values determined from a second design iteration. The second design iteration was conducted to adjust the main beam torsional stiffnesses to a practical J/I ratio of less than 4.0.

Aluminum 6061 ribs were welded to the main beam. These ribs were constructed from flat aluminum sheet stock. The heights of the ribs had to be set at nearly full aerodynamic contour so that the bending loads and shear stresses could be carried. The rib thicknesses were set at 0.032 in. for ribs at the forward seven stations and 0.06 in. for ribs at the aft three stations. Some aluminum shear material from the rib interiors was removed to reduce weight. These ribs were used to help transfer the airloads from the balsa wood aerodynamic sleeve to the main beams. The airloads pass from the rib reinforced balsa sleeve into the main beam, then through the pivot beam and into the pivot shaft.

A small aluminum "I" beam was positioned between the main beam and the root block at approximately 50% chord. This tie beam was not attached to the model root structure and added only spanwise rigidity to the model when the model pivot was located at 65% chord. The beam was fastened into the root structure when the pivot was located at 50% chord to provide an additional load path to the pivot shaft.

Mass properties were represented by over 300 distributed lumped masses in the full-scale finite element model. These masses were reduced, using mass scale factors, to wind-tunnel model scale target values of mass, static unbalance, and mass moment of inertia. Table 2 gives mass, static unbalance, and mass moment of inertia values for the model.

A beam finite element model was developed based upon the model design for use in the analysis package within the ASTROS[7,8] computer code. The model consisted of two beams with distributed stiffnesses and over 300 lump masses. The finite element model was used to predict aeroelastic characteristics of the stabilator model.

Modal and Deflection Tests

A set of load-deflection tests was performed on the wind-tunnel model to assess how the model deformations compared with scaled full-scale predicted deformation. Each of the tests was performed by placing a unit load at one of four locations: 1) the root leading edge, 2) the tip leading edge, 3) the root trailing edge, or 4) the tip trailing edge. Deflections were measured for the same locations using a dial gauge. The model performed fairly well, particularly for the root leading-edge deflection due to a load at the root leading-edge point.

Modal tests and analyses were conducted for the model to determine the model's natural frequencies and mode shapes. These modes were used to perform aeroelasticity analyses. An additional goal of the model analyses was to define the similarities and differences between the scaled targets and the model analytical and measured results. The ASTROS finite element model was used to perform modal analyses for each of three design iterations for the model. Table 3 presents model target frequencies, ASTROS predictions for each of the design iterations, and measured data from the model. The initial modal analysis conducted using the stiffness levels from the first design iteration showed good correlation between the first four out-of-plane vertical vibration modes and the vibration modes predicted by the full-scale finite element model.

Table 1 Stabilator aluminum beams' cross-sectional area moments of inertia

Main beam				Pivot beam		
	Design				Design	
Chordwise station, in.	I, II, and III I, in.^{4}	I J, in.^{4}	II and III J, in.^{4}	Spanwise station, in.	I, II, and III I, in.^{4}	I, II, and III J, in.^{4}
0.00–12.18	0.00066	0.001711	0.003422	Root-1	4.40933	4.182037
12.18–36.57	0.01092	0.028505	0.057009	1–8.29	0.38302	1.0
36.57–47.96	0.04653	0.121477	0.242954	—	—	—
47.96–54.55	0.07765	0.202719	0.405438	—	—	—
54.55–70.00	0.02529	0.066020	0.132040	—	—	—

Table 2 Mass properties for horizontal surface model

Location of mass center, leading-edge root					
X, in.	Y, in.	Mass, g	Mass unbalance (about $Y = 0$), gm-in.	Mass moment of inertia (about c.g.), gm-in.^{2}	Mass moment of inertia (about $Y = 0$), gm-in.^{2}
6.71	2.11	53.35	112.35	40.67	277.26
15.55	3.89	175.74	685.21	290.61	2,962.28
26.19	4.83	236.98	1,144.22	2,049.46	7,574.12
35.47	6.53	285.81	1,866.99	4,460.78	16,656.59
46.25	4.29	663.50	2,850.74	19,303.69	31,551.93
54.58	9.51	447.46	4,253.78	15,937.11	56,375.68
64.08	10.89	618.99	6,737.97	30,309.53	103,655.23
74.74	13.59	876.34	11,907.69	45,032.46	206,833.94
Total 53.52	8.80	3,358.17	29,558.96	165,706.09	425,886.94

Table 3 Comparison of stabilator natural frequencies, Hz

Mode	Model target with flexible spindle	ASTROS (model with flexible spindle), design 1	ASTROS (model with practical beam), design 2	ASTROS (model with practical beam and spindle), design 3	Measured sine dwell	Measured random
Rigid rotation	10.1	10.2	10.2	15.2	16.8	16.8
First chordwise bending	15.4	15.3	15.3	16.8	18.0	18.4
First chordwise torsion	32.6	32.6	29.2	34.1	51.2	51.2
Tip bending	34.5	—	—	—	34.5	—
Second chordwise bending	50.3	52.3	44.9	57.5	55.2	55.6
Second chordwise torsion	60.2	—	—	—	75.6	78.8

Table 4 Comparison of natural frequencies, Hz

	Stabilator pivot location							
	65% root chord				50% root chord			
	Spindle locked		Includes actuator		Spindle locked		Includes actuator	
Mode	ASTROS	Test	ASTROS	Test	ASTROS	Test	ASTROS	Test
Rigid rotation	15.3	16.8	9.8	9.6	15.2	14.2	8.4	8.4
First chordwise bending	16.8	18.0	16.6	18.4	20.1	22.0	19.6	22.0
First chordwise torsion	34.1	51.2	32.8	43.2	34.0	46.5	31.9	38.0
Second chordwise bending	57.5	55.2	49.3	55.6	75.6	68.9	45.9	54.4

A second modal analysis was conducted using the stiffness levels from the second design iteration. The analysis showed a reduction in the third and fourth mode natural frequencies to 29.2 and 44.9 Hz, respectively. A final modal analysis was conducted for the final design iteration. Table 4 shows natural frequency comparisons for the model with the pivot located at 50 and 65% root chord, respectively. Modal tests were conducted on the wind-tunnel model using both sine dwell and random techniques. Table 4 also depicts results from these tests for comparison with analysis.

Aeroelastic Predictions

Analyses were performed to identify aeroelastic instabilities using ASTROS and the *P-k* solution method. Doublet lattice[9] aerodynamics were used to model aerodynamic forces. Analyses were performed at Mach 0.5, 0.7, and 0.9 for both the 65% chord pivot location and the 50% chord pivot location configurations in order to determine match point aeroelastic predictions for correlation with wind-tunnel results. A doublet lattice aerodynamic box pattern consisting of 10 chordwise by 10 spanwise boxes was used.

Three separate actuation spring conditions were analyzed for the 65% configuration. These spring conditions included one condition where the spring was locked out and two conditions where the actuation spring was active in the system. With the actuation spring included, analyses were performed for the spring conditions where the actuation spring resulted in the model rigid rotation mode natural frequencies

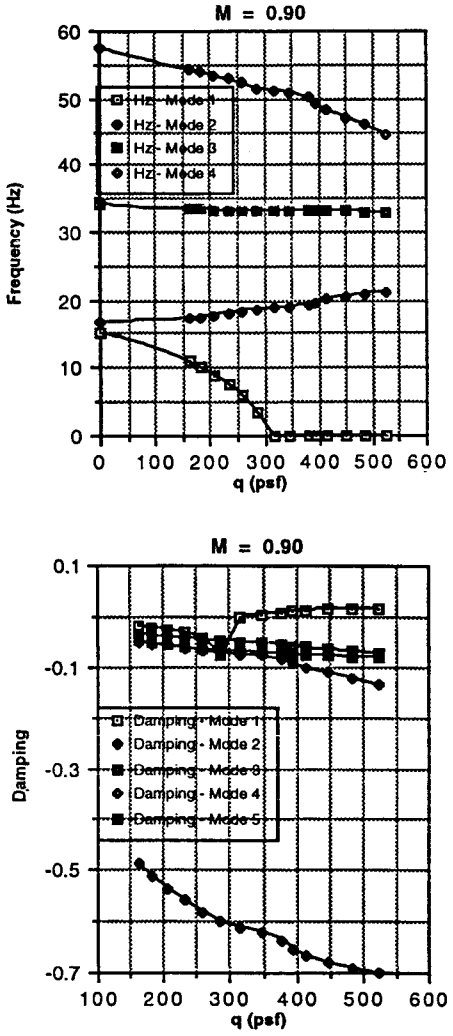

Fig. 3 *V-g* and *V-ω* plots, stabilator pivot locked at 65% root chord.

of 10 and 8 Hz for the 65% chord pivot location configuration.

For each configuration, the aeroelastic procedure predicted divergence to be the primary aeroelastic instability. The divergence dynamic pressure prediction for the 50% case is considerably higher than the predictions for the 65% case.

For each configuration, as the dynamic pressure increases, the analysis predicts the rigid rotation mode decreases in frequency until divergence results. Figure 3 depicts the *V-g* and *V-ω* plots of aeroelastic analyses for the configuration with the pivot located at 65% root chord and the actuation stiffness locked out. The first chordwise bending mode increases in frequency while the third, fourth, and fifth mode frequencies tend to decrease slightly as dynamic pressure increases.

Wind-Tunnel Tests Results

The stabilator aeroelastic model was tested in the NASA Langley 16-ft TDT. Though the model was scaled for the TDT with Freon as the test medium, actual testing was restricted to air. Using air as the test medium, wind-tunnel test data were gathered that defined the aeroelastic instability boundary for the 65% root chord pivot configuration for two actuation stiffness levels. The 50% root chord pivot configuration was also tested in air. However, limits on the dynamic pressure level when testing in air prevented the determination of an aeroelastic instability boundary for this root configuration. There were no test flutter instabilities identified for either configuration within the wind-tunnel envelope.

The primary aeroelastic instability identified during wind-tunnel testing was aeroelastic divergence. The Southwell divergence projection method[10] was the primary method used to determine the divergence dynamic pressures. Basic load data, such as the strain gauge data shown in Fig. 4, were plotted vs model angle of attack. These load data were obtained from four strain gauges located on the model's primary beams as shown in Fig. 2. Accelerometers, located fore and aft on the model, were used to monitor the model's frequency response in the airflow. Model root and turntable angle-of-attack measurements were also taken.

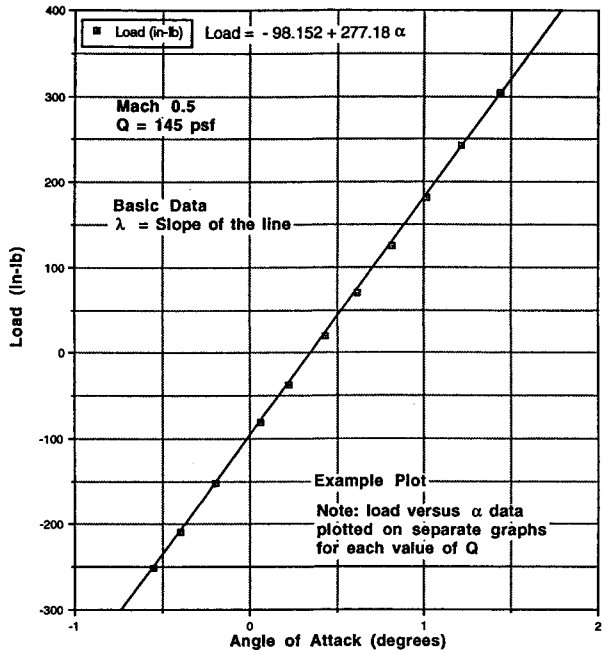

Fig. 4 Example, Southwell basic data plot.

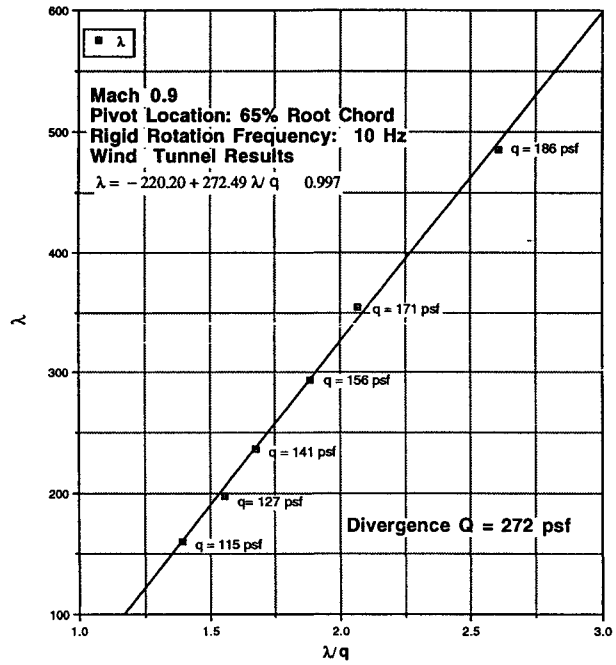

Fig. 5 Example, Southwell divergence projection method.

The Southwell divergence projection method accurately projects divergence when test dynamic pressures reach 60–90% of the actual divergence dynamic pressure. Basic strain load vs angle-of-attack data are plotted at these subcritical dynamic pressures. Slopes are calculated from least-square-fits applied to the basic load vs angle-of-attack data plots. These slopes are reduced for each dynamic pressure test point.

The slope of each load vs angle-of-attack plot is normalized by the dynamic pressure value where the data was generated. Plots depicting slope/q vs slope are developed for each Mach number. The slopes of least-square-fits of these data are the divergence projections. Figure 5 presents an example plot generated at Mach 0.9 for the 65% root chord, 10-Hz rigid rotation configuration. The slope of this slope/q vs slope plot is the projected divergence dynamic pressure at Mach 0.9. The model rigid rotation mode natural frequency, the critical aeroelastic mode, was also tracked during wind-tunnel testing. When the rigid rotation mode frequency drops to 0 Hz, static aeroelastic divergence occurs. Figure 6 depicts the tracks of the rigid rotation frequency tracking between the airflow off, model rigid rotation frequency, and the projected divergence dynamic pressure.

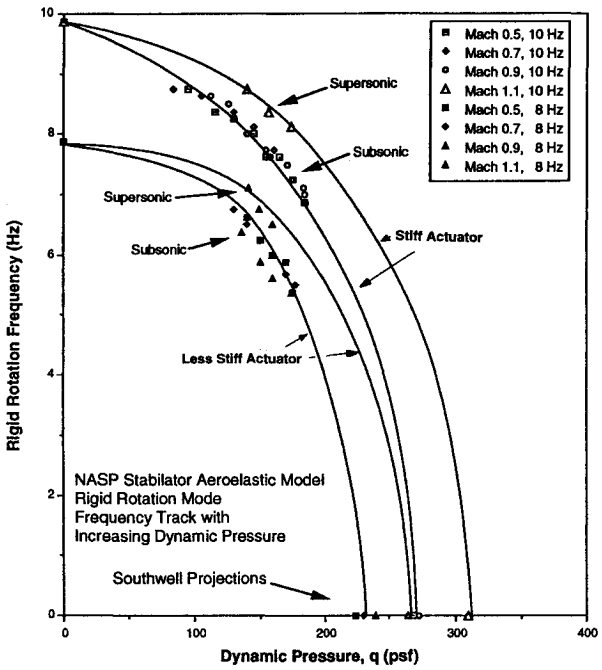

Fig. 6 Rigid rotation mode track vs dynamic pressure.

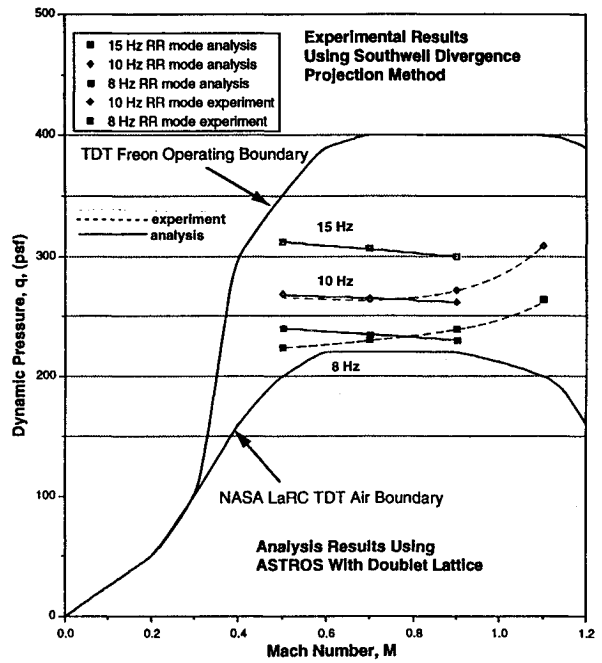

Fig. 7 Stabilator model divergence boundaries.

The stabilator model was also tested with the pivot located at the 50% root chord pivot location. The model was tested to a dynamic pressure of 270 psf at Mach 0.5. The divergence dynamic pressure was too high for subcritical divergence techniques to effectively project a divergence dynamic pressure.

Figure 7 depicts the two divergence boundaries identified for the 65% root chord pivot location model. Each of the divergence boundaries correspond to a different actuation stiffness. The higher divergence boundary was projected for the model with actuation stiffness resulting in a 10-Hz rigid rotation mode. The lower divergence boundary was projected for the model with actuation stiffness resulting in an 8-Hz rigid rotation mode. Aeroelastic divergence predictions using the ASTROS code with doublet lattice aerodynamics were conducted up to Mach 0.9 and are also shown for both configurations. No supersonic analyses were conducted.

The subsonic divergence boundaries for both configurations exhibit no transonic dip. This is most likely due to the model's 70-deg leading-edge sweep. The divergence dynamic pressures are higher at supersonic speeds than at subsonic speeds due to the aft shift in aerodynamic center with supersonic flow.

Vertical Lifting Surface Model

The transonic vertical lifting surface model consists of a stabilizer and attached rudder, a fuselage fairing, a splitter plate, and instrumentation. The vertical stabilizer has an AR of 0.29, a 70-deg leading-edge sweep, a 5-deg hinge-line sweep, and a 5-deg trailing-edge sweep. The airfoil has a sharp leading edge and is nonsymmetric, wedge-shaped, and flat on the port side. Figure 8 shows the transonic vertical stabilizer model.

The aeroelastic model is mounted to a solid steel root mount fixture that provides a rigid root boundary condition. The steel fixture was bolted at five locations to the same splitter plate used during the horizontal model tests. A nonsymmetric, aerodynamic fairing was fabricated to cover the root mount fixture and simulate the local fuselage surface interface on the port side of a twin vertical tail aircraft.

Aeroelastic Design

The vertical stabilizer and rudder model's geometric properties and overall mass and stiffness levels were derived from a full-scale hypersonic lifting surface preliminary design description present in a NASTRAN finite element model representation.

The design approach for the stabilizer model was selected based on the extreme lightweight requirement quoted in the full-scale preliminary design. The model had to weigh as little as possible, yet retain strength levels appropriate to withstand transonic loading. To simulate overall mass and stiffness requirements, the design approach relied on the use of the thinnest possible composite skins separated by the lightest available core material. Mass, strength, and stiffness levels were driven by the properties and practical gauge limits of existing materials. Aerodynamic properties were simulated by maintaining the vertical lifting surface's exterior contour

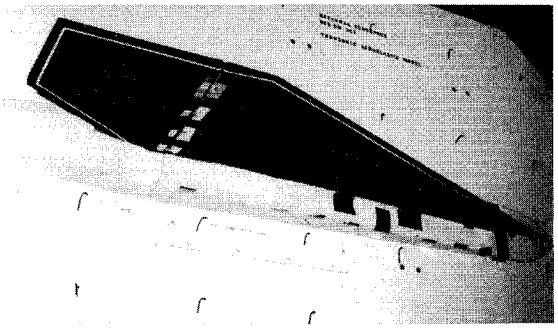

Fig. 8 Vertical lifting surface model in the wind tunnel.

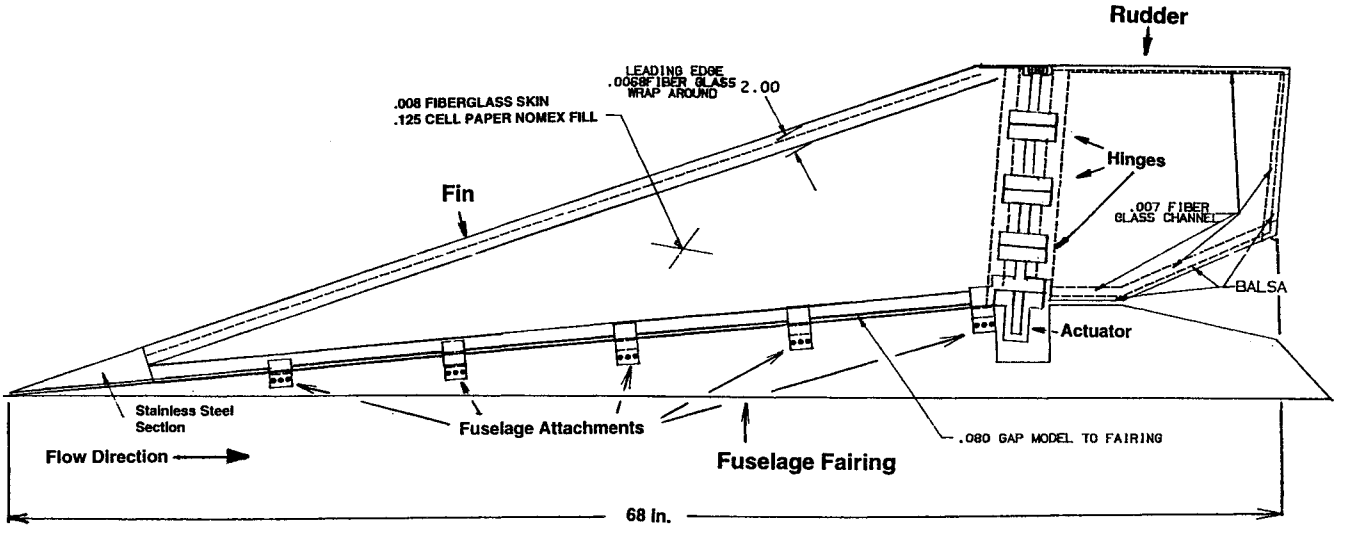

Fig. 9 Vertical stabilizer model layout.

through geometric scaling. A ballast mass was used to achieve an aeroelastic instability within the wind-tunnel envelope. A detailed layout of the vertical stabilizer wind-tunnel model is shown in Fig. 9. Five linear springs, also shown in Fig. 9, simulated fuselage attachments that connected the model root to the rigid steel mount fixture.

Paper honeycomb was selected as the core material for the sandwich construction because it provided the required level of model strength for the least total structural mass and could be machined to maintain the lifting surface's aerodynamic contour. Thin fiberglass was selected for the skins because its stiffness characteristics, when stabilized by the honeycomb core, provided an acceptable level of model stiffness to achieve an aeroelastic instability within the TDT.

The model's mass and stiffness characteristics were primarily determined by the particular honeycomb and fiberglass selected. The paper honeycomb was formed to match model geometry and exterior contour to provide proper aerodynamic forces. The fiberglass skins were made of four plies of Burlington 107 fiberglass weave. The 107 fiberglass weave has approximately three fiber strands running 0 deg for every two strands running in the 90-deg direction. Each ply of the fiberglass had a nominal thickness of 1.7 mil. The plys were stacked 0/45-45/0. The skins were temperature cured under vacuum pressure using Hysol EA 93/96 epoxy resin.

The fin and rudder cores were made from Nomex HRH-10 aramid fiber/phenolic resin honeycomb with a $\frac{1}{8}$-in. cell diameter and a 1.8-lb/ft^3 density. The honeycomb was machined to external contour by a computer numerical control (CNC) mill using a high-speed air-grinding head and a sanding disc. The $\frac{1}{8}$-in. cell size was selected to prevent fiberglass dimpling in the skin and the 1.8-lb/ft^3 density was selected to minimize weight.

After the cores were contoured, narrow contoured balsa wood strips were cemented to the perimeter of the Nomex® cores to stabilize the edges. Fiberglass channels were fabricated and placed around the perimeter of the balsa-stabilized honeycomb cores. The fiberglass channels overlapped the honeycomb core $\frac{1}{2}$ in. along the perimeter. Aluminum machined flexure fittings were placed over the fiberglass channels located along both the fin and rudder hinge line.

The fiberglass skins were placed over the core assembly and attached using Hysol® EA 93/94 epoxy resin. The skins were attached to the core assembly by vacuum bagging and curing the resin epoxy under temperature.

Actuator stiffness was provided by one of two aluminum torsion spring actuators. One actuator simulated a rigid stiffness condition, the other defined the baseline configuration and was scaled based on a practical stiffness level representative of hypersonic aircraft. The actuator was located at the root near the centerline hinge.

Finite element analyses were performed using NASTRAN to determine the vertical stabilizer's structural dynamic and aeroelastic characteristics. The analytical modeling of the vertical fin's structural characteristics was accomplished using NASTRAN due to the availability of a CHEX element that was unavailable within ASTROS.

Following fabrication, modal tests revealed that the model's mass goal was achieved, but the stiffness level was excessive. Mass ballast, in the form of a 154-g lead ballast weight, was added to the fin model aft tip to obtain an aeroelastic instability within the TDT boundary.

Modal and Deflection Tests

A set of load-deflection tests was performed on the vertical lifting surface for comparison with NASTRAN finite element model predictions. Each of the tests was performed by placing a unit load at one of five locations: 1) a point midway along the fin leading edge, 2) the fin tip leading edge, 3) the fin tip at the hinge line, 4) the rudder tip at the trailing edge, or 5) the rudder aft end at the tip. Deflections were measured at the same locations using a dial gauge. A favorable comparison was made between results from the finite element model and those from the deflection tests. Modal tests were also performed for the vertical lifting surface model to determine the model's natural frequencies and mode shapes. Table 5 presents the comparisons made between test and analysis results from NASTRAN. The results between measured model shapes and predicted mode shapes agreed well for the rudder rotation and first fin bending modes.

Aeroelastic Predictions

Analyses were performed to identify aeroelastic instabilities using the NASTRAN flutter module. The *P-k* flutter solution method was used. Doublet lattice aerodynamics were used to model aerodynamic forces. Aeroelastic analyses were performed to determine match point aeroelastic predictions for correlation with wind-tunnel results. The analyses were performed at Mach 0.3, 0.4, 0.6, 0.7, 0.8, and 0.9 for the baseline configuration.

The primary flutter instability predicted using these analyses involved coupling between the first fin bending mode and the rudder rotation mode. The flutter dynamic pressure was predicted to increase slightly with Mach number and is shown in Fig. 10. Control surface buzz was not predicted using the doublet-lattice aerodynamic method. However, empirical data was available to suggest that this fin and rudder com-

Table 5 Comparison of vertical model natural frequencies, Hz

Mode	NASTRAN	Measured
1. Rudder rotation	21.1	21.0
2. Fin first bending	34.3	35.2
3. Second fin mode	103.6	102.8
4. Third fin mode	160.6	166.2

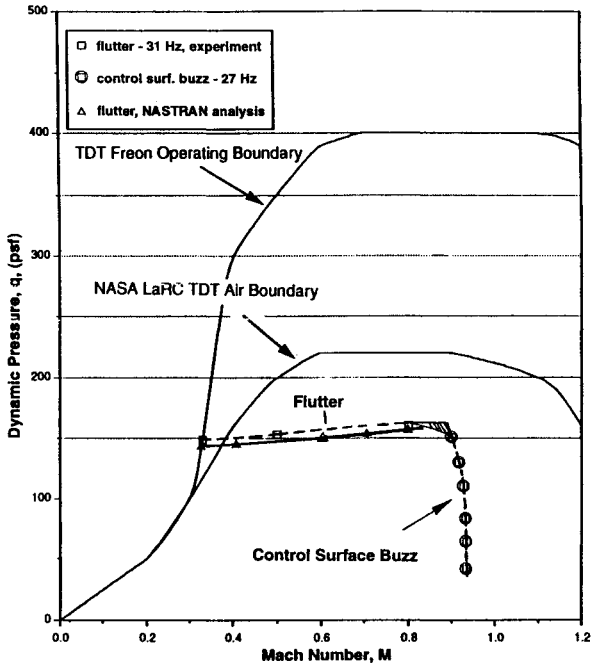

Fig. 10 Vertical fin/rudder model flutter boundaries.

bination with a 5-deg swept hinge line was subject to transonic control surface buzz.

Wind-Tunnel Tests

The vertical lifting surface aeroelastic model was tested in the NASA Langley 16-ft TDT using air as the test medium. Wind-tunnel test data were gathered to define the aeroelastic instability boundary for the baseline configuration. Two aeroelastic instabilities: 1) a mild fin/rudder flutter mode and 2) a mild control surface buzz mode, were identified.

A subcritical flutter response prediction method known as the inverse amplitude method[11] was used to plot strain gauge and accelerometer outputs to project flutter dynamic pressures. Using this method, each of the model's wind-on natural frequencies were obtained using an on-line spectrum analyzer. The frequencies were plotted vs the inverse of the frequency's amplitude to project a flutter point. However, the actual flutter and buzz modes identified during testing were sufficiently mild to permit testing at the flutter dynamic pressures.

The fin/rudder flutter mode occurred at a dynamic pressure of 150 psf across the range of subsonic speeds from Mach 0.3 to 0.9. The flutter mode boundary was fairly flat throughout the dynamic pressure envelope, rising only slightly with increasing dynamic pressure. The flutter mode's frequency, measured by strip chart recorder, was 30.5 Hz at Mach 0.4 and increased to 32 Hz as Mach number increased.

Control surface buzz began to occur at Mach 0.9 and at a dynamic pressure of 150 psf. The control surface buzz boundary intersected sharply with the flutter mode boundary. As Mach number increased to Mach 0.93, the dynamic pressure where control surface buzz occurred decreased sharply to 85 psf. The buzz mode's frequency was 27 Hz and has the greatest excitation level between Mach 0.91–0.93.

Both the fin/rudder flutter boundary and the boundary for control surface buzz are presented in Fig. 10. The experimental flutter boundary was successfully predicted using NASTRAN with subsonic doublet lattice aerodynamics. Control surface buzz predictions require a nonlinear transonic aerodynamic method and were not made.

The flutter and control surface buzz trends noted in the wind tunnel for this specific scaled hypersonic model agree well with test trends observed on other generic hypersonic configurations.[12] This empirical data showing that highly swept planforms with unswept hinge lines will experience control surface buzz proved an adequate predictor.

Conclusions

Transonic lifting surface component aeroelastic wind-tunnel models were designed and fabricated by Wright Laboratory and tested in the NASA Langley Research Center TDT. Stiffness tests, modal tests, and proof load tests were conducted for both models. The horizontal lifting surface model exhibited scaled aeroelastic responses representative of a full-scale preliminary design of a hypersonic lifting surface stabilator. The vertical lifting surface model was geometrically scaled and designed aeroelastically to obtain flutter within the wind-tunnel boundaries.

The horizontal lifting surface model's aeroelastic instability was identified as static aeroelastic divergence. The Southwell method was used to project the stabilator's divergence dynamic pressures in the wind tunnel. No flutter instabilities were identified. Aeroelastic analyses conducted using subsonic doublet-lattice aerodynamics were able to predict the divergence instability boundaries satisfactorily. Both wind-tunnel test and aeroelastic analyses indicate divergence dynamic pressures of approximately 230, 260, or 300 psf, depending on the model pivot actuation stiffness level.

The decreasing rigid rotation frequency of the stabilator may pose a problem when the stabilator is attached to a lifting body. The rigid rotation frequency could potentially couple with any one of several lifting body modes to produce a body freedom flutter instability.

The vertical lifting surface's aeroelastic instabilities were identified as mild fin/rudder flutter and mild control surface buzz. The mild aeroelastic instabilities were excited directly in the wind tunnel. Aeroelastic analyses conducted using subsonic doublet-lattice aerodynamics were able to satisfactorily predict the fin/rudder flutter instability involving coupling between the model's first and second natural modes. Both test and analyses indicated fin/rudder flutter to occur at approximately 31 Hz at dynamic pressures from 150 to 160 psf across the subsonic speed range.

Control surface buzz began to occur at Mach 0.9 and at a dynamic pressure of 150 psf. As Mach number increased to Mach 0.93, the buzz dynamic pressure decreased sharply to 85 psf. Control surface buzz predictions require a nonlinear aerodynamics method and were not made.

The flutter and control surface buzz trends noted in the wind tunnel for this specific scaled hypersonic model agree well with test trends observed on other generic hypersonic configurations.[12–16] This empirical data, showing that highly swept planforms with unswept hinge lines will experience control surface buzz, proved a good predictor. The data further suggests that increases in leading-edge sweep and airfoil thickness are likely to increase the Mach number at which buzz occurs. Application of a seal in the area of the hinge gap gives a destabilizing trend. An increase in the sweep of the control surface hinge line may be one solution to reduce susceptibility to transonic buzz.

Overall, the test and analyses results from these models suggest that aeroelastic predictions for planforms with such high sweeps may be satisfactorily analyzed using existing subsonic aerodynamic theories up to Mach 0.9. Above Mach 0.9, care must be taken to avoid aeroelastic problems caused by

shock waves. At transonic Mach numbers, the horizontal lifting surface model divergence dynamic pressure was unaffected by the transonic shocks. However, the vertical lifting surface model's control surface buzz was the result of an oscillating shock condition.

Acknowledgments

The authors wish to thank L. Wasserman for his technical advice concerning the design of the aeroelastic models and W. Pitman and L. Mantia for their work fabricating the models. Additional thanks go to B. Cramer for his work with the vertical model composite skins. The authors also wish to thank M. Farmer, Nancy Thompson, R. Ricketts, and the NASA Langley test team for their significant efforts during wind-tunnel testing of these models. A special thanks is given to S. Harris and R. Snyder for their assistance with model testing during the course of the effort.

References

[1]Reed, W. H., Hanson, P. W., and Alford, W. J., "Assessment of Flutter Model Testing Relating to the National Aero-Space Plane," NASA CR 1002, July 1987.

[2]Rainey, A. G., "Aeroelastic Research at High Speed," Joint Conference on Lifting Manned Hypervelocity and Re-Entry Vehicles, Pt. I, NASA Langley Research Center, Hampton, VA, 1960.

[3]*The NASTRAN User's Manual*, Level 17.5, Computer Software Management and Information Center (COSMIC), Univ. of Georgia, Athens, GA, Dec. 1978.

[4]Roark, R. J., *Formulas for Stress and Strain*, McGraw–Hill, New York, 1965.

[5]Bisplinghoff, R. L., Ashley, H., and Halfman, R. L., *Aeroelasticity*, Addison–Wesley, Reading, MA, Nov. 1957.

[6]Smilg, B., and Wasserman, L., "Application of Three Dimensional Flutter Theory to Aircraft Structures," Air Force Technical Rept., AFTR-4798, July 1942.

[7]Neill, D. J., Johnson, E. H., and Canfield, R., "ASTROS—A Multidisciplinary Automated Structural Design Tool," AIAA Paper 87-0713, April 1987.

[8]Neill, D., Johnson, E., and Herendeen, D., "Automated Structural Optimization System (ASTROS)," Vol. II, User's Manual, Air Force Wright Aeronautical Labs., AFWAL-TR-88-3028, April 1988.

[9]Giesing, J. P., Kalman, T. P., and Rodden, W. P., "Subsonic Unsteady Aerodynamics for General Configurations," Air Force Flight Dynamics Lab., AFFDL-TR-71-5, April 1972.

[10]Ricketts, R. H., and Doggett, R. V., "Wind-Tunnel Experiments on Divergence of Forward-Swept Wings," NASA TP 1685, Aug. 1980.

[11]Ruhlin, C. L., Watson, J. J., Ricketts, R. H., and Doggett, R. V., "Evaluation of Four Subcritical Response Methods for On-Line Prediction of Flutter Onset in Wind Tunnel Tests," *Journal of Aircraft*, Vol. 20, No. 10, 1983, pp. 835–840.

[12]Parker, E. C., Spain, C. V., and Soistmann, D. L., "Aileron Buzz Investigated on Several Generic NASP Wing Configurations," AIAA Paper 91-0936, April 1991.

[13]Pendleton, E. W., Harris, S. R., Keller, D., and Farmer, M., "A NASP Stabilator Transonic Aeroelastic Model," *Proceedings of the NASP Technology Review* (Monterey, CA), 1993 (Paper 10).

[14]Pendleton, E. W., Moster, G. E., and Farmer, M., "Transonic Aeroelastic Models of Hypersonic Highly Swept Lifting Surface Models: Design, Analyses, and Test," AIAA Paper 94-1489, April 1994.

[15]Spain, C. V., Zeiler, T. A., Gibbons, M. D., Soistman, D. L., Pozefsky, P., DeJesus, R. O., and Brannon, C. P., "Aeroelastic Character of a National Aerospace Plane Demonstrator Concept," AIAA Paper 93-1314, April 1993.

[16]Spain, C. V., Zeiler, T. A., Bullock, E. P., and Hodge, J. S., "A Flutter Investigation of All-Moveable NASP-Like Wings at Hypersonic Speeds," AIAA Paper 93-1315, April 1993.

From writing clerical procedures to nuclear power plant procedures....
this book provides step-by-step help!

Procedure Writing Principles and Practices

Douglas Wieringa, Christopher Moore, and Valerie Barnes

Procedures are instructions, and this book explains how to write instructions so that others can understand them. Procedures can range from simple to complex; they describe anything from booting up a personal computer to operating a nuclear power plant during an emergency. Plans, mission statements, proposals, and technical articles are not procedures, although parts of these documents may be considered procedures if they present instructions. No matter how simple or complex the procedure is, certain principles govern the way it should be written. The authors draw on their more than ten years of experience and present their principles in this book.

1993, 211 pages, Paperback
ISBN 0-935470-68-9, $29.95, Order #: PPP-1(945)

Place your order today! Call 1-800/682-AIAA

AIAA
American Institute of Aeronautics and Astronautics
Publications Customer Service, 9 Jay Gould Ct., P.O. Box 753, Waldorf, MD 20604
FAX 301/843-0159 Phone 1-800/682-2422 9 a.m. - 5 p.m. Eastern

Sales Tax: CA residents, 8.25%; DC, 6%. For shipping and handling add $4.75 for 1-4 books (call for rates for higher quantities). Orders under $100.00 must be prepaid. Foreign orders must be prepaid and include a $20.00 postal surcharge. Please allow 4 weeks for delivery. Prices are subject to change without notice. Returns will be accepted within 30 days. Non-U.S. residents are responsible for payment of any taxes required by their government.